

Accurate Gauge-Invariant Tensor Network Simulations for Abelian Lattice Gauge Theory in (2+1)D

Yantao Wu^{1,*} and Wen-Yuan Liu^{2,†}

¹*Institute of Physics, Chinese Academy of Sciences, Beijing 100190, China*

²*Institute for Advanced Study in Physics, Zhejiang University, Hangzhou 310027, China*

(Dated: April 10, 2025)

We propose a novel tensor network method to achieve accurate and efficient simulations of Abelian lattice gauge theories (LGTs) in (2+1)D. The first key is to identify a gauge canonical form (GCF) of gauge-invariant tensor network states, which already simplifies existing algorithms for (1+1)D LGTs. The second key is to employ the GCF of projected entangled-pair state (PEPS) combining with variational Monte Carlo, enabling efficient variational optimization for (2+1)D LGT ground states with gauge and matter fields. We demonstrate the versatile capability of this approach for accurate simulation of pure \mathbb{Z}_2 , \mathbb{Z}_3 and \mathbb{Z}_4 gauge theory, odd- \mathbb{Z}_2 gauge theories, and \mathbb{Z}_2 gauge theory coupled to hard-core bosons, on square lattices up to 32×32 . Our work establishes gauge-invariant PEPS as a powerful approach to simulate (2+1)D Abelian LGTs.

Introduction. The study of lattice gauge theories (LGTs) constitutes a cornerstone in modern physics. They play foundational roles in quantum chromodynamics for studying quark confinement and hadron structure [1–3], and also provide critical insights into condensed matter physics, where low-energy effective theories of strongly correlated systems such as quantum spin liquids and topological orders have gauge structures [4, 5]. The traditional Monte Carlo sampling of partition functions is a very successful computational paradigm for LGTs, however, its applicability is severely limited in regimes plagued by sign problems [6]. These limitations have spurred intense efforts to develop alternative approaches such as quantum simulations [7–11].

Tensor network states (TNS) have emerged as a promising, sign-free classical simulation approach for LGT [12–23]. In (1+1)D, TNS in the form of matrix product state (MPS), has been established as a reliable numerical methodology [14, 24–28]. Extending to (2+1)D, projected entangled pair state (PEPS) [29] provides a compelling theoretical framework of LGTs [13, 17, 27, 30, 31]. Nevertheless, PEPS-based simulations face substantial challenges stemming from both the intrinsic complexity of higher-dimensionality and the rigorous requirements of gauge constraints. Recent explorations using gauge invariant Gaussian PEPS [32–35] and non-gauge-constrained PEPS [36] have made first attempts, while confronting challenges: the former suffers from accuracy restrictions imposed by Gaussian constraints, and the latter faces difficulties in variational optimization and generalization to other gauge groups or matter fields. Advancing high-precision PEPS methodologies capable of tackling generic LGTs is both a critical challenge and a fundamental necessity, given the power of PEPS to characterize strongly correlated quantum matter.

In this work, we develop a PEPS-based computational framework to achieve accurate simulations of a wide range of (2+1)D Abelian LGTs. A key element is the identification of a gauge canonical form (GCF) for

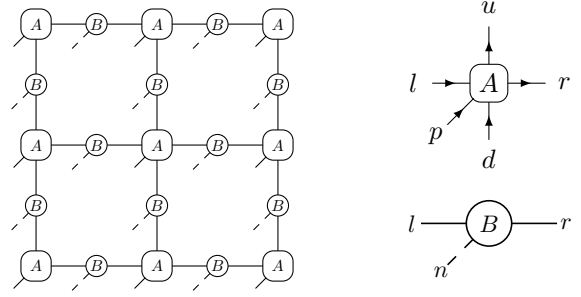


FIG. 1. Left is a diagram of a gauge-invariant PEPS for LGTs. Right are the matter tensor A and gauge tensor B . Here d is the down-leg of A , and not the spatial dimension.

gauge-invariant (GI) TNS, with which we can already significantly simplify MPS-based methods in (1+1)D. In (2+1)D, the GCF enables a particularly efficient treatment of GI-PEPS via variational Monte Carlo (VMC), facilitating precise ground-state calculations. Our method is extensively validated with simulations of \mathbb{Z}_2 , \mathbb{Z}_3 and \mathbb{Z}_4 pure gauge theory, odd- \mathbb{Z}_2 gauge theory, and \mathbb{Z}_2 gauge theory coupled to hard-core bosons, on square lattices up to 32×32 . These results establish PEPS as a powerful pathway for accurate TNS simulations of (2+1)D Abelian LGTs, providing a new tool for non-perturbatively studying LGTs and benchmarking quantum simulations.

Hamiltonian. We briefly review the LGT Hamiltonians [19, 37]. A $(d+1)$ D LGT is defined on a d -dimensional cubic lattice, with gauge fields on the links and matter fields on the vertices. For an Abelian gauge group \mathbb{Z}_N (or $U(1)$), the link Hilbert space is spanned by the eigenstates $|n\rangle$ of an electric field operator E such that $E|n\rangle = n|n\rangle$, $n \in \mathbb{Z}_N$ (or \mathbb{Z}). Its raising operator $U \equiv e^{i\phi}$ is the exponential of its canonical conjugate operator ϕ : $[\phi, E] = i$ and $U|n\rangle = |n+1 \bmod N\rangle$. The matter Hilbert space hosts a boson or a fermion on the vertex \mathbf{x} with annihilation operator $c_{\mathbf{x}}$. The gauge in-

variance, at every \mathbf{x} , is enforced as

$$c_{\mathbf{x}}^\dagger c_{\mathbf{x}} + \sum_{\alpha=1}^d (E_{(\mathbf{x}-\mathbf{e}_\alpha, \alpha)} - E_{(\mathbf{x}, \alpha)}) = Q_{\mathbf{x}} \bmod N, \quad (1)$$

where (\mathbf{x}, α) is a link between \mathbf{x} and $\mathbf{x} + \mathbf{e}_\alpha$, with \mathbf{e}_α being the unit vector along the α -th axis. $Q_{\mathbf{x}}$ is a preset integer, fixing the gauge sector. The LGT Hamiltonian is:

$$H = H_M + H_B + H_E, \quad (2)$$

$$H_M = \sum_{\mathbf{x}} m_{\mathbf{x}} c_{\mathbf{x}}^\dagger c_{\mathbf{x}} + \sum_{\mathbf{x}, \alpha} (J c_{\mathbf{x}}^\dagger U_{(\mathbf{x}, \alpha)} c_{\mathbf{x}+\mathbf{e}_\alpha} + h.c.), \quad (3)$$

$$H_B = -h \sum_{\mathbf{x}} U_{\mathbf{x},1} U_{\mathbf{x}+\mathbf{e}_1,2} U_{\mathbf{x}+\mathbf{e}_2,1}^\dagger U_{\mathbf{x},2}^\dagger + h.c., \quad (4)$$

$$H_E = g \sum_{\mathbf{x}, \alpha} 2 - 2 \cos(2\pi E_{(\mathbf{x}, \alpha)} / N) \text{ or } g \sum_{\mathbf{x}, \alpha} E_{(\mathbf{x}, \alpha)}^2, \quad (5)$$

where $m_{\mathbf{x}}$ is the chemical potential (or the bare particle mass), and J is the gauge-matter coupling strength. H_B and H_E are respectively the magnetic and electric energy terms. H_B is present only for $d \geq 2$, and the two instances of H_E are for either the \mathbb{Z}_N or $U(1)$ gauge group.

Gauge-invariant TNS. Gauge-invariant tensor network states naturally describe the physical Hilbert space of LGTs [12–15, 17, 27, 30, 31]. To construct a GI-TNS wavefunction, one works in the basis of particle occupation number and electric fields. As in Fig. 1, the network has three-leg B tensors for gauge fields and $(2d+1)$ -leg A tensors for matter fields. Gauge invariance of the wavefunction is enforced by imposing sparsity constraints on A and B . Specifically, we assign charges $q(j)$ in \mathbb{Z}_N (or \mathbb{Z}) to tensor indices j on each virtual leg, then in two spatial dimensions, tensor blocks of A and B satisfy [14]

$$A_{lrdu}^p = \mathcal{A}_{lrdu}^p \delta_{p+q(l)+q(d)-q(r)-q(u), Q_{\mathbf{x}}}, \quad (6)$$

$$B_{lr}^n = \mathcal{B}_{lr}^n \delta_{n,q(l)} \delta_{n,q(r)}. \quad (7)$$

The bond dimension of the TNS is then $D = \sum_k D_k$, where D_k is the degeneracy of the charge sector k , i.e. the number of tensor indices j with $q(j) = k$. Although this GI ansatz has been known for a decade, and its MPS algorithms has been established in (1+1)D [14], the algorithmic feasibility of GI-PEPS including optimization for ground states and computation of physical quantities, has remained a major roadblock, preventing the power of PEPS from manifesting for (2+1)D LGTs. Below we show how to overcome these challenges.

Gauge canonical form. A key ingredient for our approach is the GCF, which we now identify. On the link connecting an A tensor and a B tensor, one can define the following block-diagonal matrix:

$$X = \bigoplus_{k \in \mathbb{Z}_N \text{ (or } \mathbb{Z})} \mathcal{B}^{[k]} \quad (8)$$

where $\mathcal{B}^{[k]}$ is a $D_k \times D_k$ matrix obtained from choosing $n = k$ in B_{lr}^n and restricting to the l and r indices with charges equal to k . Using gauge transformations $A \rightarrow AX, B \rightarrow X^{-1}B$, the gauge tensor B simplifies as

$$B_{lr}^n = \delta_{lr} \delta_{n,q(l)} \delta_{n,q(r)}, \quad (9)$$

and A keeps the same form as Eq.(6). We refer to this new form as the GCF, in which the B tensors no longer contain variational parameters and one only needs to optimize the A tensors. Below we show how GCF enables efficient computations of GI-MPS and GI-PEPS.

(1+1)D. The GCF implies that during a GI-TNS calculation, one does not keep track of the gauge tensors. This already has implications in 1D. In Ref. [14], where GI-MPS was used to study the Schwinger model [38] with the $U(1)$ gauge group, the gauge and matter tensors were grouped together and the gauge field was manually cut off at $|n|_{\max} = 3$, giving an MPS with a local physical dimension 14. With GCF, we simplify the calculation by disregarding the gauge tensors and using an MPS whose local physical dimension is only 2, and cutting off the gauge field based on the entanglement spectrum. We explain this in detail in the End Matter.

(2+1)D and VMC. In 2D, GI-PEPS simulations are challenging due to their intrinsic complexity, gauge-invariance constraints, and the four-body plaquette terms in the Hamiltonian [Eq. (4)] [36]. We find that combining VMC and GCF overcomes these challenges effectively. In VMC, the expectation value of an observable is calculated as $\langle O \rangle = \sum_{\mathbf{s}} \frac{|\langle \mathbf{s} | \Psi \rangle|^2}{\langle \Psi | \Psi \rangle} \frac{\langle \mathbf{s} | O | \Psi \rangle}{\langle \mathbf{s} | \Psi \rangle}$, where $|\mathbf{s}\rangle$ labels a configuration of gauge and matter fields. This sum is estimated via sampling $|\mathbf{s}\rangle$ from the probability distribution $\frac{|\langle \mathbf{s} | \Psi \rangle|^2}{\langle \Psi | \Psi \rangle}$, where the basic component is evaluating single-layer networks $\langle \mathbf{s} | \Psi \rangle$ [39–43]. We only sample physical configurations, as unphysical ones' amplitudes are exactly zero in GI-PEPS.

The sampling and GCF critically simplifies computations: each configuration $|\mathbf{s}\rangle$ uniquely selects a single charge sector of matter tensors A with gauge tensors B absent. Thus, tensors in the resulting network $\langle \mathbf{s} | \Psi \rangle$ only have bond dimension D_k , significantly reduced from the total bond dimension $D = \sum_{k=1}^N D_k$ for \mathbb{Z}_N gauge group. This allows efficient computations using advanced PEPS-VMC techniques [42–45] that have been used to study frustrated spin systems [46–51]. See SM [52] for more discussions.

We use gradient-based stochastic reconfiguration [45, 53–55] to variationally minimize the energy of GI-PEPS for systems on the open square lattice. The computational cost scales as $O(D_k^5 \chi^2 + D_k^4 \chi^2 + D_k^3 \chi^3)$, dominated by plaquette term evaluations and variational boundary MPS compression. χ is the cutoff bond dimension of the boundary MPS for contracting $\langle \mathbf{s} | \Psi \rangle$, with $\chi = 3D_k$ being good enough. Then the energy measurement scales as $O(MN_{\text{site}} D_k^7)$, where N_{site} is the size and M is the num-

TABLE I. Ground state energy per site. The top part shows QMC and GI-PEPS ($D = 4$) energy comparison for $16 \times 16 \mathbb{Z}_2$ LGT. The rest shows the D -convergence of GI-PEPS energy at critical points for the largest sizes, i.e. $24 \times 24 \mathbb{Z}_3$ LGT and $20 \times 20 \mathbb{Z}_4$ LGT, respectively.

\mathbb{Z}_2	QMC	PEPS
$g = 0.30$	-0.76400(3)	-0.763973(8)
$g = 0.31$	-0.73841(6)	-0.738443(6)
$g = 0.32$	-0.71400(7)	-0.714032(8)
$g = 0.33$	-0.69091(7)	-0.690923(6)
$g = 0.34$	-0.6691(1)	-0.669161(6)
$g = 0.35$	-0.6486(1)	-0.648714(6)
\mathbb{Z}_3	$D = 6$	$D = 9$
$g = 0.375$	-0.548401(6)	-0.548409(4)
\mathbb{Z}_4	$D = 8$	$D = 12$
$g = 0.33$	-0.712554(8)	-0.712557(4)

ber of Monte Carlo sweeps [52] typically on the order of 10^4 with statistical uncertainty about 10^{-5} .

Pure \mathbb{Z}_N gauge theory. We first consider pure $\mathbb{Z}_2 - \mathbb{Z}_4$ gauge theories (no matter field, $Q_{\mathbf{x}} \equiv 0$). We use $D_k = 2$ which we find is good enough for convergence on relevant sizes (see Table I), resulting in total PEPS bond dimension $D = 4, 6, 8$, correspondingly. Fixing $h = 1$, we scan g to compute ground state properties. It is known that the \mathbb{Z}_2 LGT undergoes a continuous deconfined-confined phase transition, while \mathbb{Z}_3 experiences a first-order one [56].

The \mathbb{Z}_2 pure gauge theory can be simulated unbiasedly by quantum Monte Carlo (QMC) via duality to the transverse field Ising model. Shown in Table I, near the critical point $g_c \simeq 0.3285$ [57], PEPS energies agree excellently with QMC, indicating $D_k = 2$ well converges the results. Here QMC has slightly larger uncertainties due to critical slowing-down, whereas wavefunction-based PEPS show minimal sampling uncertainties due to the variance vanishing principle [52]. The behavior of Wilson loop operators on the 32×32 lattice (see SM [52]), is also consistent with a deconfinement phase transition at g_c .

For the \mathbb{Z}_3 case, we compute ground-state properties for sizes from 8×8 to 24×24 . The first derivative of energy, $\frac{\partial \langle H \rangle}{\partial g} = \frac{1}{g} \langle H_E \rangle$ [Fig. 2(a)], and its finite-difference second derivative $\frac{\partial^2 \langle H \rangle}{\partial g^2}$ [Fig. 2(b)], reveal clear signatures of a first-order transition, consistent with early studies [56]. The transition point from small sizes shows a minor shift. The convergence between 20×20 and 24×24 yields a thermodynamic-limit critical point at $g_c = 0.375(3)$. This agrees very well with a recently found $g_c = 0.37(1)$ using neural quantum states on torus up to size 10×10 [58]. This is to be compared with the non-gauge-constrained iPEPS result $g_c = 0.448(3)$ [36], where the quantitative difference may arise from the reliance of iPEPS on simple update optimization rather than the fully variational optimization employed here,

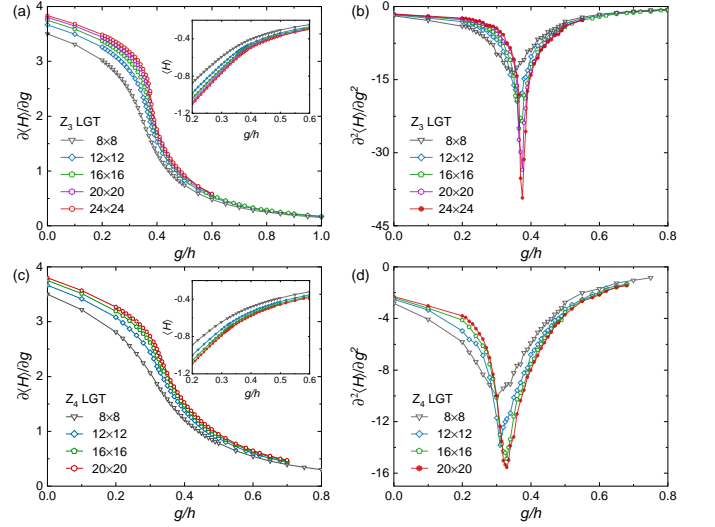


FIG. 2. Results of \mathbb{Z}_3 (a-b), \mathbb{Z}_4 (c-d) LGTs at various g , including ground state energy $\langle H \rangle$ [insets of (a) and (c)], the first-order and second-order energy derivative.

demonstrating the challenge of such calculations.

For the \mathbb{Z}_4 case, unexplored previously by TNS, we extend our analysis to 20×20 sites. As shown in Figs. 2(c,d), the energy derivatives suggest a phase transition at $g_c = 0.330(5)$, by comparing results from size 16×16 and 20×20 . This constitutes the first PEPS study of \mathbb{Z}_4 LGT, offering a benchmark for higher-order gauge groups. Very interestingly, this g_c overlaps with that of the \mathbb{Z}_2 theory, 0.3285 . In fact, for the 3D classical gauge theories, the \mathbb{Z}_4 theory is proven to be equivalent to the $\mathbb{Z}_2 \times \mathbb{Z}_2$ theory [59]. While no proof is available in the quantum case, we *conjecture* here that the equivalence still holds.

Odd- \mathbb{Z}_2 theory. Another representative example is the odd \mathbb{Z}_2 gauge theory, i.e. with $Q_{\mathbf{x}} \equiv 1$ for all \mathbf{x} , relevant for understanding spin liquids and dimer models [60–64]. According to theoretical predictions [61–63], by varying g it experiences a continuous transition between a deconfined phase and a confined phase that breaks translation symmetry. Its dual model - the fully frustrated transverse field Ising model [62], has been studied by QMC [65]. With GI-PEPS, we are able to directly obtain its ground state *wavefunction*. Figs. 3(a) and (b) show the plaquette operator $P_{\mathbf{x}} = U_{\mathbf{x},1} U_{\mathbf{x}+\mathbf{e}_1,2} U_{\mathbf{x}+\mathbf{e}_2,1}^\dagger U_{\mathbf{x},2}^\dagger + h.c.$ on a 32×32 lattice, revealing a uniform and a symmetry broken phase at $g = 0.4$ and 0.8 , respectively.

To precisely locate the transition point, we compute the valence-bond solid (VBS) order parameter [48]

$$D_{x/y} = \frac{1}{L(L-1)} \sum_{\mathbf{x}} (-1)^{x_\alpha} \bar{E}_{\mathbf{x}}^\alpha, \quad (10)$$

where $\alpha = 1, 2$ for D_x, D_y . $\bar{E}_{\mathbf{x}}^\alpha = 2 - 2 \cos(\pi E_{(\mathbf{x}, \alpha)})$ is the electric field strength on the link (\mathbf{x}, α) [see Eq.(5)],

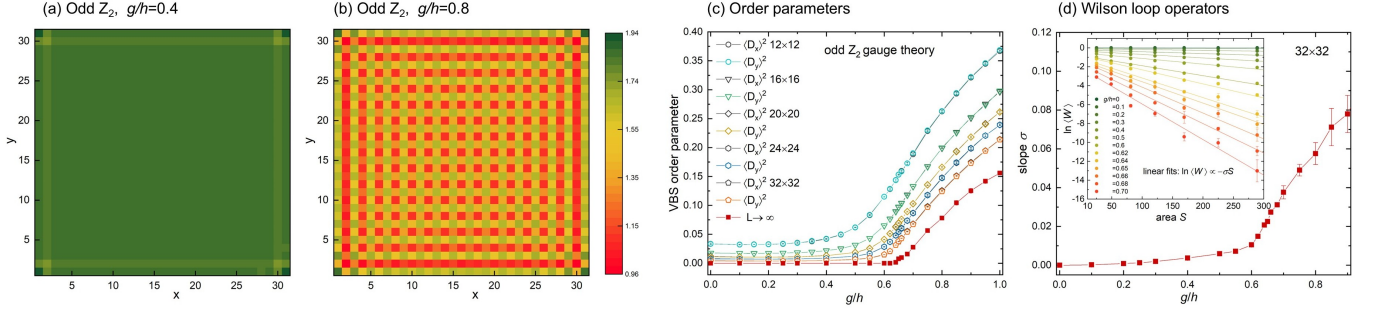


FIG. 3. Results of odd \mathbb{Z}_2 LGT. (a) and (b) present the plaquette value $\langle P_x \rangle$ at each site \mathbf{x} on 32×32 at $g/h = 0.4$ and 0.8 . (c) shows the VBS order parameters $\langle D_x \rangle^2$ (black) and $\langle D_y \rangle^2$ (colorful), and red symbols are the values in thermodynamic limit extrapolated using quadratic fits of $\langle D_x \rangle^2$. The inset of (d) is the linear-linear plot of $\ln \langle W \rangle$ versus area S (different central regions on 32×32) to extract σ following $\langle W \rangle \propto e^{-\sigma S}$; the main panel shows the g -dependence of the slope σ .

and $\mathbf{x} = (x_1, x_2)$ is the vertex position. Note the identical $\langle D_x \rangle^2$ and $\langle D_y \rangle^2$ in Fig. 3(c), which reflects the C_4 rotation symmetry. Through quadratic finite-size extrapolation, we obtain VBS order parameters in the thermodynamic limit [red curve in Fig. 3(c)], locating the phase transition point at $g_c = 0.64(1)$, in good agreement with the QMC results $g_c \simeq 0.634$ from the dual model [65].

The Wilson loop operator $\langle W \rangle$ on the 32×32 lattice is shown in Fig. 3(d). The slope σ , extracted from $\langle W \rangle \propto e^{-\sigma S}$, remains small for $g \lesssim 0.6$ but increases sharply afterward, signaling a perimeter-law to area-law transition consistent with $g_c = 0.64(1)$. These nonlocal operator calculations complements those of local operators $D_{x/y}$ in detecting translation symmetry breaking, providing insight into the underlying physics from the perspective of deconfinement.

\mathbb{Z}_2 gauge theory coupled to hard-core bosons. Finally we demonstrate that we can directly deal with matter fields. Here we consider \mathbb{Z}_2 gauge fields coupled to hard-core bosons. Its (1+1)D version has been studied, known as the \mathbb{Z}_2 Bose-Hubbard model [66], while the (2+1)D case remains uncharted. For benchmarking with exact diagonalization (ED) calculation, we first consider a 3×3 square lattice with 2 bosons. The definite boson number is realized by sampling in the corresponding particle number subspace. Taking $(h, g, J) = (1, 0.33, 0.5)$ as an example, the optimized $D = 6$ PEPS gives the energy persite $-0.470713502(3)$ using $M = 10^5$ samples, matching the ED energy -0.4707135061 excellently.

We then scale up to 16×16 sites at half filling of bosons. Fig. 4(a) presents the energies from PEPS with bond dimensions D up to 14 for different sizes at $(h, g, J) = (1, 0.33, 0.5)$. Unlike the pure \mathbb{Z}_2 LGT where $D = 4$ is sufficient for convergence, the matter-coupled case requires $D = 12$. These results reflect the increased entanglement of this model and our ability to handle large bond dimensions. We also compare the thermodynamic-limit energy evaluated using different central bulk energies for extrapolations [43, 48]. Shown in Fig. 4(b), given a central bulk region of $L_b \times L_b$ [52], for example, $L_b = L - 2$,

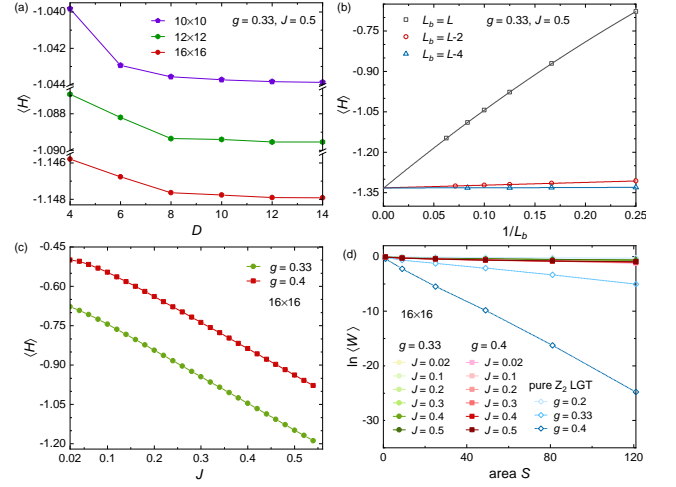


FIG. 4. Results of \mathbb{Z}_2 gauge field coupled to hard-core bosons at half-filling ($h = 1$). (a) Convergence of energy with respect to bond dimensions. (b) Finite-size scaling of the energy using central bulk $L_b \times L_b$ energy of an $L \times L$ lattice. Quadratic fits are used for extrapolations. (c) J -dependence of energy at $g = 0.33$ and 0.4 on 16×16 lattice. (d) Wilson loop operators on 16×16 lattice at different J for a given $g = 0.33$ (green) and $g = 0.4$ (red), compared to the pure \mathbb{Z}_2 LGT (blue). The green and red lines are respectively largely overlapped, both very close to the pure \mathbb{Z}_2 LGT at $g = 0.2$ (lightest blue).

the extrapolated energy for the thermodynamic limit is $-1.3322(4)$, in good agreement with those from other choices of $L_b = L$ and $L_b = L - 4$ that are $-1.3337(4)$ and $-1.3322(2)$, respectively. This consistency corroborates our results [43, 48].

One also expects that, in the presence of dynamical matter fields, the Wilson loop operator exhibits a perimeter-law even in the confinement regime of the pure \mathbb{Z}_2 LGT, due to screening by the matter field [67]. This is indeed what we observe. We present the energy and Wilson loop operator of 16×16 lattice in Figs. 4(c) and (d). For pure \mathbb{Z}_2 LGT, as shown previously, $g = 0.2, 0.33$ and 0.4 correspond to the deconfined, near critical and

confined regimes, respectively. From Fig. 4(d) we see after adding matter fields, at $g = 0.33$ and 0.4 , Wilson loop operators for different J show perimeter-law behavior.

Conclusion and discussion. We have developed a powerful gauge-invariant tensor network computational framework for (2+1)D Abelian LGTs, overcoming long-standing challenges in algorithmic feasibility of GI-PEPS. Central to our approach is the gauge canonical form, which fixes gauge tensors to parameter-free forms—thereby reducing variational parameters exclusively to matter tensors, as well as its further combination with VMC. We validate the framework across diverse models and achieve large-scale simulations up to 32×32 sites. These advances establish GI-PEPS as a state-of-the-art tool for (2+1)D Abelian LGTs. We leave the generalization to fermionic matter to future work.

The potential of GI-PEPS and GCF remains to be seen for double-layer TNS methods [68]. Another possibility recently proposed is to modify the GI-PEPS ansatz as a symmetric PEPS by embedding the gauge group G into an enlarged globally symmetric theory with group $G \times G$ [69].

Acknowledgement. We are grateful to Akira Matsumoto for sending us the ED value of the Schwinger model. Y.W. would like to thank discussion with Akira Matsumoto, Etsuko Itou, Masazumi Honda, and Tetsuo Hatsuda during the early stage of the work. W.Y.L. is especially grateful to Garnet K. Chan for encouragement. Y.W. was supported by the RIKEN iTHEMS fellowship, and is currently supported by a start-up grant from the Institute of Physics at Chinese Academy of Sciences. W.Y.L. is supported by a start-up grant from Zhejiang University. Part of the code is implemented based on the TenPy code base [70, 71].

END MATTER

GCF in (1+1)D. In the End Matter, we demonstrate that the GCF enables an elegant algorithm of the time evolution block decimation (TEBD) [72] for LGT in (1+1)D. We take the Schwinger model as an example, which is a toy-model of quantum electrodynamic in (1+1)D [38]. Its Hamiltonian is $H_M + H_E$ with $U(1)$ gauge group and staggered fermions $Q_x = (1 + (-1)^x)/2$ and $m_x = (-1)^x m$.

Due to the GCF, simulations do not explicitly require the gauge tensors. Instead, the time evolution of the Schwinger model is simulated via a $U(1)$ -symmetric TEBD applied to the Hamiltonian with global symmetry:

$$H = \sum_x m_x c_x^\dagger c_x + \sum_x J c_x^\dagger c_{x+1} + h.c., \quad (11)$$

with an MPS made only of A tensors. The would-be gauge canonical B tensors dictate that the virtual charges

of A encode the physical electric fields. Instead of using Jordan-Wigner transformation, we directly use the fermionic MPS in the swap gate formalism [73, 74].

Simulating Eq. (11) is different from the LGT systems in three aspects:

1. The electric part $H_E = g \sum_x E_x^2$ is missing.
2. The hopping $c_x^\dagger c_{x+1}$ is different from the gauge-invariant hopping $c_x^\dagger U_x c_{x+1}$.
3. For systems with global symmetry, there is an arbitrariness in the symmetry charge of the MPS tensors A_x . Suppose one has tensor A_x and A_{x+1} , with symmetry charge Q_x and Q_{x+1} . Combining A_x and A_{x+1} gives a two-site tensor $\Lambda \equiv A_x A_{x+1}$, with symmetry charge $Q_x + Q_{x+1}$. The TEBD gate tensor U changes Λ to Λ' , but does not change the symmetry charge of Λ . When one splits Λ' to A'_x and A'_{x+1} via singular value decomposition, one can assign any symmetry charge Q'_x to A'_x as long as A'_{x+1} 's symmetry charge is then assigned as $Q_x + Q_{x+1} - Q'_x$, and the virtual charge on the link between x and $x+1$ properly redefined. This arbitrariness is absent for LGTs, as the symmetry charge Q_x is pre-defined.

To accommodate these differences, two additions are needed during the TEBD of Eq. (11):

1. At each link, apply the time evolution gate $e^{-i d\tau g E_x^2}$ [Eq. (5)] ($d\tau$ being the time step) on the virtual charges of A_x
2. Keep the symmetry charge of A_x as Q_x when splitting a two-site wavefunction $A_x A_{x+1}$. During the TEBD of Eq.(11), the hopping term $c_x^\dagger c_{x+1}$ shifts the symmetry charge of A_x (A_{x+1}) by $+1$ (-1). One can exploit the gauge freedom of the symmetry charges in an MPS with global symmetry to redefine the post-split tensors' symmetry charges — reverting A_x 's to Q_x and A_{x+1} 's to Q_{x+1} — while incrementing the virtual charge between x and $x+1$ by $+1$. This precisely implements the gauge invariant $c_x^\dagger U_x c_{x+1}$, as summarized in the Fact 1.

Fact 1. Let A'_x and A'_{x+1} be the result of $c_x^\dagger c_{x+1}$ acting on the two-site wavefunction $A_x A_{x+1}$:

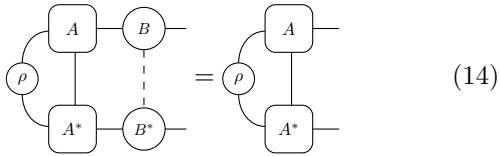
$$\begin{array}{c} \text{---} [A'_x] \text{---} [A'_{x+1}] \text{---} \\ | \qquad \qquad | \\ \text{---} [A_x] \text{---} [A_{x+1}] \text{---} \\ | \qquad \qquad | \\ \text{---} c_x^\dagger c_{x+1} \text{---} \end{array} \quad (12)$$

Then

$$\begin{array}{c} \text{---} [A_x] \text{---} [B] \text{---} [A_{x+1}] \text{---} \\ | \qquad \vdots \qquad | \\ \text{---} [A'_x] \text{---} [B] \text{---} [A'_{x+1}] \text{---} \\ | \qquad \vdots \qquad | \\ \text{---} c_x^\dagger U_{(x,1)} c_{x+1} \text{---} \end{array} \quad (13)$$

where B is in GCF.

Another important piece of the TEBD algorithm is the MPS isometric canonical form (not to be confused with the gauge canonical form): the truncation of the two-site wavefunction must be performed at the canonical center. The isometric canonical form is also preserved by the CGF due to the following equation:



provided that B is in GCF.

The approach described here significantly simplifies the algorithm of Ref. [14], which required manual gauge field truncation and blocking of A and B tensors. For example, if one cuts the gauge field at $|n|_{\max} = 3$, then a physical leg dimension of 14 is needed on each site in [14], while for us the physical dimension is always 2. In addition, our cutoff of the gauge field is based on entanglement via SVD, which seems much more natural for an MPS.

To validate our method, we perform imaginary-time evolution ($d\tau = 0.01$) on a 16-site chain with $m = 0.2$, $J = -5i$, $g = 0.05$, and obtained ground state energy -36.33990 , which is in excellent agreement with exact diagonalization (-36.33994) [75]. Fig. 5 further illustrates real-time evolution starting from the vacuum state: particle-antiparticle pairs are spontaneously created, and smaller fermion masses m enhance particle-antiparticle pair production, directly manifesting the Schwinger mechanism [38].

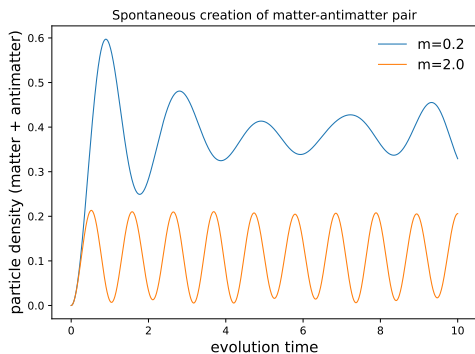


FIG. 5. Schwinger mechanism on a 40-site chain. $J = i$, $g = 1$. The time evolution is obtained using TEBD with a second-order Trotter decomposition with time step $dt = 0.01$.

* equal contribution; yantaow@iphy.ac.cn

† equal contribution; wylu@zju.edu.cn

- [1] K. G. Wilson, Confinement of quarks, *Phys. Rev. D* **10**, 2445 (1974).
- [2] J. B. Kogut, An introduction to lattice gauge theory and spin systems, *Rev. Mod. Phys.* **51**, 659 (1979).
- [3] K. Fukushima and T. Hatsuda, The phase diagram of dense qcd, *Reports on Progress in Physics* **74**, 014001 (2010).
- [4] X.-G. Wen, *Quantum Field Theory of Many Body Systems: From the origin of sound to an origin of light and electrons* (Oxford University Press, New York, 2004).
- [5] A. Kitaev, Anyons in an exactly solved model and beyond, *Annals of Physics* **321**, 2 (2006).
- [6] M. Troyer and U.-J. Wiese, Computational complexity and fundamental limitations to fermionic quantum monte carlo simulations, *Phys. Rev. Lett.* **94**, 170201 (2005).
- [7] C. Gross and I. Bloch, Quantum simulations with ultracold atoms in optical lattices, *Science* **357**, 995 (2017).
- [8] C. D. Bruzewicz, J. Chiaverini, R. McConnell, and J. M. Sage, Trapped-ion quantum computing: Progress and challenges, *Applied Physics Reviews* **6** (2019).
- [9] P. Krantz, M. Kjaergaard, F. Yan, T. P. Orlando, S. Gustavsson, and W. D. Oliver, A quantum engineer's guide to superconducting qubits, *Applied physics reviews* **6** (2019).
- [10] B. Yang, H. Sun, R. Ott, H.-Y. Wang, T. V. Zache, J. C. Halimeh, Z.-S. Yuan, P. Hauke, and J.-W. Pan, Observation of gauge invariance in a 71-site Bose-Hubbard quantum simulator, *Nature* **587**, 392 (2020).
- [11] M. C. Banuls, R. Blatt, J. Catani, A. Celi, J. I. Cirac, M. Dalmonte, L. Fallani, K. Jansen, M. Lewenstein, S. Montangero, *et al.*, Simulating lattice gauge theories within quantum technologies, *The European physical journal D* **74**, 1 (2020).
- [12] L. Tagliacozzo and G. Vidal, Entanglement renormalization and gauge symmetry, *Phys. Rev. B* **83**, 115127 (2011).
- [13] L. Tagliacozzo, A. Celi, and M. Lewenstein, Tensor networks for lattice gauge theories with continuous groups, *Phys. Rev. X* **4**, 041024 (2014).
- [14] B. Buyens, J. Haegeman, K. Van Acoleyen, H. Verschelde, and F. Verstraete, Matrix product states for gauge field theories, *Phys. Rev. Lett.* **113**, 091601 (2014).
- [15] P. Silvi, E. Rico, T. Calarco, and S. Montangero, Lattice gauge tensor networks, *New Journal of Physics* **16**, 103015 (2014).
- [16] H. Zou, Y. Liu, C.-Y. Lai, J. Unmuth-Yockey, L.-P. Yang, A. Bazavov, Z. Y. Xie, T. Xiang, S. Chandrasekharan, S.-W. Tsai, and Y. Meurice, Progress towards quantum simulating the classical $O(2)$ model, *Phys. Rev. A* **90**, 063603 (2014).
- [17] J. Haegeman, K. Van Acoleyen, N. Schuch, J. I. Cirac, and F. Verstraete, Gauging quantum states: From global to local symmetries in many-body systems, *Phys. Rev. X* **5**, 011024 (2015).
- [18] Y. Kuramashi and Y. Yoshimura, Three-dimensional finite temperature \mathbb{Z}_2 gauge theory with tensor network scheme, *Journal of High Energy Physics* **2019**, 1 (2019).
- [19] P. Emonts and E. Zohar, Gauss law, minimal coupling and fermionic PEPS for lattice gauge theories, *SciPost Phys. Lect. Notes*, 12 (2020).
- [20] T. Felser, P. Silvi, M. Collura, and S. Montangero, Two-dimensional quantum-link lattice quantum electrodynamics at finite density, *Phys. Rev. X* **10**, 041040 (2020).

- [21] G. Magnifico, T. Felser, P. Silvi, and S. Montangero, Lattice quantum electrodynamics in (3+1)-dimensions at finite density with tensor networks, *Nature communications* **12**, 3600 (2021).
- [22] Y. Meurice, R. Sakai, and J. Unmuth-Yockey, Tensor lattice field theory for renormalization and quantum computing, *Rev. Mod. Phys.* **94**, 025005 (2022).
- [23] G. Cataldi, G. Magnifico, P. Silvi, and S. Montangero, Simulating (2 + 1)D SU(2) Yang-Mills lattice gauge theory at finite density with tensor networks, *Phys. Rev. Res.* **6**, 033057 (2024).
- [24] T. Byrnes, P. Sriganesh, R. Bursill, and C. Hamer, Density matrix renormalisation group approach to the massive schwinger model, *Nuclear Physics B - Proceedings Supplements* **109**, 202 (2002).
- [25] T. M. R. Byrnes, P. Sriganesh, R. J. Bursill, and C. J. Hamer, Density matrix renormalization group approach to the massive schwinger model, *Phys. Rev. D* **66**, 013002 (2002).
- [26] M. C. Bañuls, K. Cichy, J. I. Cirac, and K. Jansen, The mass spectrum of the schwinger model with matrix product states, *Journal of High Energy Physics* **2013**, 1 (2013).
- [27] E. Rico, T. Pichler, M. Dalmonte, P. Zoller, and S. Montangero, Tensor networks for lattice gauge theories and atomic quantum simulation, *Phys. Rev. Lett.* **112**, 201601 (2014).
- [28] M. Carmen Bañuls and K. Cichy, Review on novel methods for lattice gauge theories, *Reports on Progress in Physics* **83**, 024401 (2020).
- [29] F. Verstraete and J. I. Cirac, Renormalization algorithms for quantum-many body systems in two and higher dimensions, *arXiv:cond-mat/0407066* (2004).
- [30] E. Zohar, M. Burrello, T. B. Wahl, and J. I. Cirac, Fermionic projected entangled pair states and local U(1) gauge theories, *Annals of Physics* **363**, 385 (2015).
- [31] E. Zohar and M. Burrello, Building projected entangled pair states with a local gauge symmetry, *New Journal of Physics* **18**, 043008 (2016).
- [32] E. Zohar and J. I. Cirac, Combining tensor networks with monte carlo methods for lattice gauge theories, *Phys. Rev. D* **97**, 034510 (2018).
- [33] P. Emonts, A. Kelman, U. Borla, S. Moroz, S. Gazit, and E. Zohar, Finding the ground state of a lattice gauge theory with fermionic tensor networks: A $2 + 1d$ \mathbb{Z}_2 demonstration, *Phys. Rev. D* **107**, 014505 (2023).
- [34] P. Emonts, M. C. Bañuls, I. Cirac, and E. Zohar, Variational Monte Carlo simulation with tensor networks of a pure \mathbb{Z}_3 gauge theory in 2+1 D, *Phys. Rev. D* **102**, 074501 (2020).
- [35] A. Kelman, U. Borla, I. Gomelski, J. Elyovich, G. Roose, P. Emonts, and E. Zohar, Gauged gaussian projected entangled pair states: A high dimensional tensor network formulation for lattice gauge theories, *Phys. Rev. D* **110**, 054511 (2024).
- [36] D. Robaina, M. C. Bañuls, and J. I. Cirac, Simulating 2+1 D \mathbb{Z}_3 lattice gauge theory with an infinite projected entangled-pair state, *Phys. Rev. Lett.* **126**, 050401 (2021).
- [37] J. Kogut and L. Susskind, Hamiltonian formulation of wilson's lattice gauge theories, *Phys. Rev. D* **11**, 395 (1975).
- [38] J. Schwinger, Gauge invariance and mass. ii, *Phys. Rev.* **128**, 2425 (1962).
- [39] A. W. Sandvik and G. Vidal, Variational quantum Monte Carlo simulations with tensor-network states, *Phys. Rev. Lett.* **99**, 220602 (2007).
- [40] N. Schuch, M. M. Wolf, F. Verstraete, and J. I. Cirac, Simulation of quantum many-body systems with strings of operators and Monte Carlo tensor contractions, *Phys. Rev. Lett.* **100**, 040501 (2008).
- [41] L. Wang, I. Pizorn, and F. Verstraete, Monte Carlo simulation with tensor network states, *Phys. Rev. B* **83**, 134421 (2011).
- [42] W.-Y. Liu, S.-J. Dong, Y.-J. Han, G.-C. Guo, and L. He, Gradient optimization of finite projected entangled pair states, *Phys. Rev. B* **95**, 195154 (2017).
- [43] W.-Y. Liu, Y.-Z. Huang, S.-S. Gong, and Z.-C. Gu, Accurate simulation for finite projected entangled pair states in two dimensions, *Phys. Rev. B* **103**, 235155 (2021).
- [44] W.-Y. Liu, S.-J. Du, R. Peng, J. Gray, and G. K.-L. Chan, Tensor network computations that capture strict variationality, volume law behavior, and the efficient representation of neural network states, *Phys. Rev. Lett.* **133**, 260404 (2024).
- [45] W.-Y. Liu, H. Zhai, R. Peng, Z.-C. Gu, and G. K.-L. Chan, Accurate simulation of the Hubbard model with finite fermionic projected entangled pair states, *arXiv:2502.13454* (2025).
- [46] W.-Y. Liu, S. Dong, C. Wang, Y. Han, H. An, G.-C. Guo, and L. He, Gapless spin liquid ground state of the spin- $\frac{1}{2}$ $J_1 - J_2$ heisenberg model on square lattices, *Phys. Rev. B* **98**, 241109 (2018).
- [47] W.-Y. Liu, S.-S. Gong, Y.-B. Li, D. Poilblanc, W.-Q. Chen, and Z.-C. Gu, Gapless quantum spin liquid and global phase diagram of the spin-1/2 $J_1 - J_2$ square antiferromagnetic Heisenberg model, *Science Bulletin* **67**, 1034 (2022).
- [48] W.-Y. Liu, J. Hasik, S.-S. Gong, D. Poilblanc, W.-Q. Chen, and Z.-C. Gu, Emergence of gapless quantum spin liquid from deconfined quantum critical point, *Phys. Rev. X* **12**, 031039 (2022).
- [49] W.-Y. Liu, S.-S. Gong, W.-Q. Chen, and Z.-C. Gu, Emergent symmetry in quantum phase transition: From deconfined quantum critical point to gapless quantum spin liquid, *Science Bulletin* **69**, 190 (2024).
- [50] W.-Y. Liu, D. Poilblanc, S.-S. Gong, W.-Q. Chen, and Z.-C. Gu, Tensor network study of the spin- $\frac{1}{2}$ square-lattice $J_1 - J_2 - J_3$ model: Incommensurate spiral order, mixed valence-bond solids, and multicritical points, *Phys. Rev. B* **109**, 235116 (2024).
- [51] W.-Y. Liu, X.-T. Zhang, Z. Wang, S.-S. Gong, W.-Q. Chen, and Z.-C. Gu, Quantum criticality with emergent symmetry in the extended shastry-sutherland model, *Phys. Rev. Lett.* **133**, 026502 (2024).
- [52] Y. Wu and W.-Y. Liu, Supplemental material (2025).
- [53] S. Sorella, Green function monte carlo with stochastic reconfiguration, *Phys. Rev. Lett.* **80**, 4558 (1998).
- [54] E. Neuscamman, C. J. Umrigar, and G. K.-L. Chan, Optimizing large parameter sets in variational quantum monte carlo, *Phys. Rev. B* **85**, 045103 (2012).
- [55] T. Vieijra, J. Haegeman, F. Verstraete, and L. Vanderstraeten, Direct sampling of projected entangled-pair states, *Phys. Rev. B* **104**, 235141 (2021).
- [56] G. Bhanot and M. Creutz, Phase diagram of Z(N) and U(1) gauge theories in three dimensions, *Phys. Rev. D* **21**, 2892 (1980).
- [57] F. Wu, Y. Deng, and N. Prokof'ev, Phase diagram of the

- toric code model in a parallel magnetic field, *Phys. Rev. B* **85**, 195104 (2012).
- [58] A. Apte, C. Córdova, T.-C. Huang, and A. Ashmore, Deep learning lattice gauge theories, *Phys. Rev. B* **110**, 165133 (2024).
 - [59] H. Grosse, C. Lang, and H. Nicolai, Equivalence of the z_4 and the $z_2 \times z_2$ lattice gauge theories, *Physics Letters B* **98**, 69 (1981).
 - [60] R. A. Jalabert and S. Sachdev, Spontaneous alignment of frustrated bonds in an anisotropic, three-dimensional ising model, *Phys. Rev. B* **44**, 686 (1991).
 - [61] T. Senthil and M. P. A. Fisher, Z_2 gauge theory of electron fractionalization in strongly correlated systems, *Phys. Rev. B* **62**, 7850 (2000).
 - [62] R. Moessner, S. L. Sondhi, and E. Fradkin, Short-ranged resonating valence bond physics, quantum dimer models, and ising gauge theories, *Phys. Rev. B* **65**, 024504 (2001).
 - [63] S. Sachdev, Topological order, emergent gauge fields, and fermi surface reconstruction, *Reports on Progress in Physics* **82**, 014001 (2018).
 - [64] Z. Yan, R. Samajdar, Y.-C. Wang, S. Subir, and Z. Y. Meng, Triangular lattice quantum dimer model with variable dimer density, *Nature communications* **13**, 5799 (2022).
 - [65] S. Wenzel, T. Coletta, S. E. Korshunov, and F. Mila, Evidence for columnar order in the fully frustrated transverse field ising model on the square lattice, *Phys. Rev. Lett.* **109**, 187202 (2012).
 - [66] D. González-Cuadra, A. Dauphin, P. R. Grzybowski, P. Wójcik, M. Lewenstein, and A. Bermudez, Symmetry-breaking topological insulators in the \mathbb{Z}_2 bose-hubbard model, *Phys. Rev. B* **99**, 045139 (2019).
 - [67] E. Fradkin, *Fideld Theories of Condensed Matter Physics* (Cambridge University Press, 2013).
 - [68] We would like to thank Jutho Haegeman for sending us a recent unpublished master thesis from his group, where exact gradient descent using automatic differentiation was attempted for finding the ground states of an infinite-PEPS with structure similar to GCF. Although the numerical results are yet to converge with the bond dimension in the thesis, they do show the possibility of such calculations using more conventional methods based on double-layer TNS contraction.
 - [69] M. Canals, N. Chepiga, and L. Tagliacozzo, A tensor network formulation of lattice gauge theories based only on symmetric tensors, *arXiv:2412.16961* (2024).
 - [70] J. Hauschild and F. Pollmann, Efficient numerical simulations with tensor networks: Tensor network python (tenpy), *SciPost Physics Lecture Notes* , 005 (2018).
 - [71] J. Hauschild, J. Unfried, S. Anand, B. Andrews, M. Bintz, U. Borla, S. Divic, M. Drescher, J. Geiger, M. Hefel, K. Hémerly, W. Kadow, J. Kemp, N. Kirchner, V. S. Liu, G. Möller, D. Parker, M. Rader, A. Romen, S. Scalet, L. Schoonderwoerd, M. Schulz, T. Soejima, P. Thoma, Y. Wu, P. Zechmann, L. Zweng, R. S. K. Mong, M. P. Zaletel, and F. Pollmann, Tensor network Python (TeNPy) version 1, *SciPost Phys. Codebases* , 41 (2024).
 - [72] G. Vidal, Efficient classical simulation of slightly entangled quantum computations, *Phys. Rev. Lett.* **91**, 147902 (2003).
 - [73] Q.-Q. Shi, S.-H. Li, J.-H. Zhao, and H.-Q. Zhou, Graded projected entangled-pair state representations and an algorithm for translationally invariant strongly correlated electronic systems on infinite-size lattices in two spatial dimensions, *arXiv preprint arXiv:0907.5520* (2009).
 - [74] P. Corboz, R. Orús, B. Bauer, and G. Vidal, Simulation of strongly correlated fermions in two spatial dimensions with fermionic projected entangled-pair states, *Phys. Rev. B* **81**, 165104 (2010).
 - [75] Provided by Akira Matsumoto.
 - [76] S.-J. Dong, C. Wang, Y. Han, G.-c. Guo, and L. He, Gradient optimization of fermionic projected entangled pair states on directed lattices, *Phys. Rev. B* **99**, 195153 (2019).
 - [77] S.-J. Dong, C. Wang, Y.-J. Han, C. Yang, and L. He, Stable diagonal stripes in the t - J model at $\bar{n}_h = 1/8$ doping from fPEPS calculations, *npj Quantum Materials* **5**, 28 (2020).
 - [78] F. Becca and S. Sorella, *Quantum Monte Carlo Approaches for Correlated Systems* (Cambridge University Press, 2017).
 - [79] F. Verstraete, V. Murg, and J. I. Cirac, Matrix product states, projected entangled pair states, and variational renormalization group methods for quantum spin systems, *Advances in Physics* **57**, 143 (2008).

Supplemental Material

S-1. Variational Monte Carlo

There are standard works about the variational Monte Carlo algorithm for tensor network states [34, 39–41]. It has been used in generic bosonic PEPS and fermionic PEPS for solving frustrated spin and fermionic models [42–51, 76, 77], as well as gauged Gaussian PEPS for lattice gauge theories [32–35]. Here we follow the presentation for generic PEPS in Ref. [42, 43], and discuss its application for gauge-invariant PEPS.

In VMC, using $|\mathbf{s}\rangle \equiv |\mathbf{n}, \mathbf{p}\rangle$ to denote gauge field configuration $|\mathbf{n}\rangle$ and matter field configuration $|\mathbf{p}\rangle$, the expectation values are computed by importance sampling of configurations $|\mathbf{s}\rangle$. For example, the total energy reads:

$$E_{\text{tot}} = \frac{\langle \Psi | H | \Psi \rangle}{\langle \Psi | \Psi \rangle} = \sum_{\mathbf{s}} \frac{|\langle \mathbf{s} | \Psi \rangle|^2}{\langle \Psi | \Psi \rangle} \frac{\langle \mathbf{s} | H | \Psi \rangle}{\langle \mathbf{s} | \Psi \rangle} = \sum_{\mathbf{s}} p(\mathbf{s}) E_{\text{loc}}(\mathbf{s}) , \quad (\text{S1})$$

where $\langle \mathbf{s} | \Psi \rangle$ is the amplitude of the configuration $|\mathbf{s}\rangle$, and $p(\mathbf{s}) = |\langle \mathbf{s} | \Psi \rangle|^2 / \langle \Psi | \Psi \rangle$ is the probability. $E_{\text{loc}}(\mathbf{s})$ is the local energy defined as

$$E_{\text{loc}}(\mathbf{s}) = \frac{\langle \mathbf{s} | H | \Psi \rangle}{\langle \mathbf{s} | \Psi \rangle} = \sum_{\mathbf{s}'} \frac{\langle \mathbf{s}' | \Psi \rangle}{\langle \mathbf{s} | \Psi \rangle} \langle \mathbf{s} | H | \mathbf{s}' \rangle . \quad (\text{S2})$$

The sampling process in Eq.(S1) employs the conventional Markov Chain Monte Carlo (MCMC) method. Beginning with the initial configuration $|\mathbf{s}_0\rangle$, a trial configuration $|\mathbf{s}_1\rangle$ is proposed. According to the Metropolis algorithm, this candidate configuration $|\mathbf{s}_1\rangle$ is accepted as the new configuration for the Markov Chain if a uniformly random number in $[0,1]$ is below the probability ratio $p(\mathbf{s}_1)/p(\mathbf{s}_0)$. If rejected, another configuration state $|\mathbf{s}'_1\rangle$ is proposed instead.

Monte Carlo sampling provides a direct framework for calculating energy gradients:

$$g_i = 2\langle E_{\text{loc}}(\mathbf{s}) O_i(\mathbf{s}) \rangle - 2\langle E_{\text{loc}}(\mathbf{s}) \rangle \langle O_i(\mathbf{s}) \rangle , \quad (\text{S3})$$

where $\langle \dots \rangle$ means the Monte Carlo average. This enables efficient wavefunction optimization via stochastic gradient descent or stochastic reconfiguration. Detailed implementations are discussed in Refs. [42, 43, 45].

A critical feature of VMC arises from the *vanishing energy variance principle* for ground states. For energy eigenstates, i.e. $H|\Psi\rangle = E_g|\Psi\rangle$, the energy variance $\text{var}\langle H \rangle = \langle H^2 \rangle - \langle H \rangle^2 = 0$. In the context of Monte Carlo sampling, for energy eigenstates it has $E_{\text{loc}}(\mathbf{s}) = \langle \mathbf{s} | H | \Psi \rangle / \langle \mathbf{s} | \Psi \rangle = E_g$, which is independent of configurations $|\mathbf{s}\rangle$. Near the ground state, this property allows accurate energy estimation with minimal sampling noise, even using small sample sizes [78]. This is indeed what we observe, for example, in the comparison between PEPS and QMC results for the pure \mathbb{Z}_2 LGT presented in the main text.

S-2. VMC for gauge-invariant PEPS

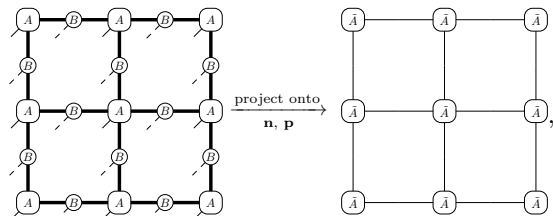
Below we outline key considerations for implementing variational Monte Carlo (VMC) with gauge-invariant PEPS, focusing on amplitude computation and Markov chain configuration sampling.

Amplitude computations. The gauge-invariant PEPS $|\Psi\rangle$ inherently eliminates unphysical configurations: Any configuration $|\bar{\mathbf{s}}\rangle$ violating the gauge symmetry has $\langle \bar{\mathbf{s}} | \Psi \rangle = 0$, enforced by the block-sparse structure of PEPS tensors. For physical configurations $|\mathbf{s}\rangle \equiv |\mathbf{n}, \mathbf{p}\rangle$, considering the gauge canonical form, the gauge constraint requires

$$\text{mod}(p + n_l + n_d - n_u - n_r, N) = Q_{\mathbf{x}} \quad (\text{S4})$$

at each vertex \mathbf{x} for \mathbb{Z}_N gauge group, where p denotes matter configuration, and n_l, n_u, n_r, n_d represent gauge configurations on adjacent links..

The amplitude $\langle \mathbf{s} | \Psi \rangle$ for a physical configuration $|\mathbf{s}\rangle \equiv |\mathbf{n}, \mathbf{p}\rangle$ corresponds to a tensor network:



$$(\text{S5})$$

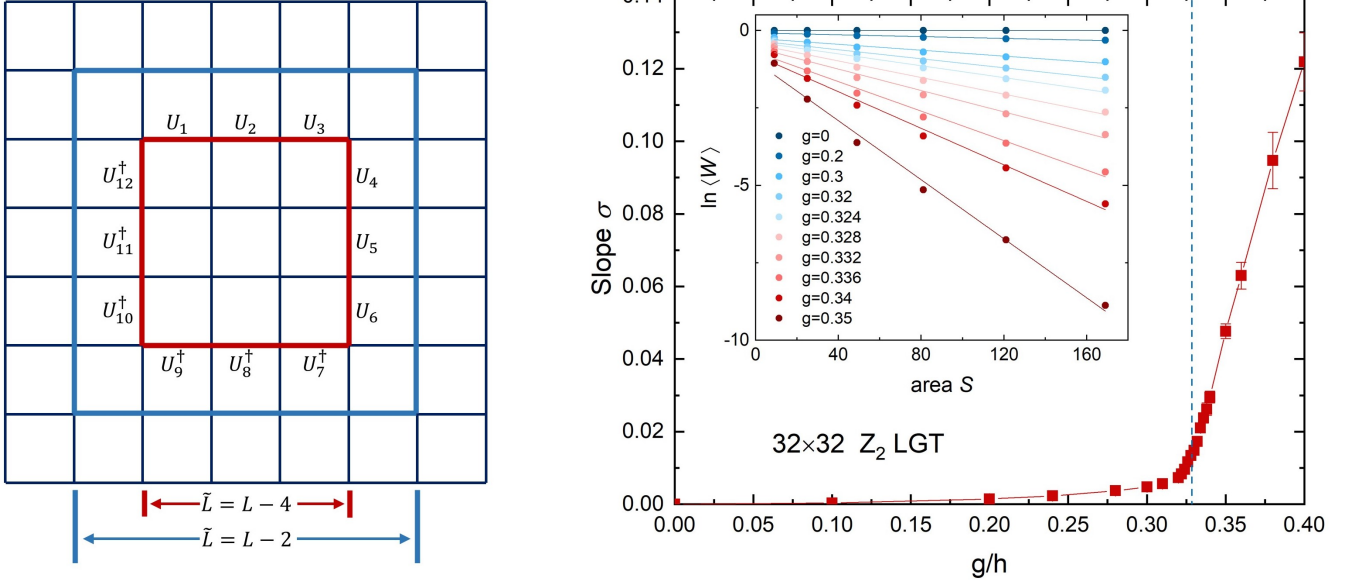


FIG. S1. Left: Computing Wilson loop operators around a central square $\tilde{L} \times \tilde{L}$ on a given open boundary square lattice $L \times L$. Two different closed paths (red and blue) are highlighted, with corresponding area $S = 9$ and $S = 25$. Right: The behavior of Wilson loop operator for \mathbb{Z}_2 LGT on a 32×32 lattice. The inset shows the linear fits of $\ln \langle W \rangle \propto -\sigma S$ to extracted the slope σ ; the main panel shows the variation of σ with g/h increasing, and the vertical blue dashed line denotes the critical point $g_c \simeq 0.3285$ from quantum Monte Carlo [57].

where gauge symmetry reduces each tensor A to a single sector \tilde{A} , with B absent due to gauge canonical form. This reduces the bond dimension of amplitude networks to D_k , compared to the full PEPS bond dimension $D = \sum_k D_k$. The amplitude network are efficiently contracted using standard methods like SVD or variational compression [79].

Configuration sampling. The sampling starts by randomly selecting an initial configuration $|\mathbf{s}_0\rangle$ that satisfy the gauge constraint: For every vertex \mathbf{x} in the \mathbb{Z}_N gauge theory, the condition $\text{mod}(p + n_l + n_d - n_u - n_r, N) = Q_{\mathbf{x}}$ must hold. To generate a trial gauge configuration $|\mathbf{s}_1\rangle$, the plaquette operator $P_{\mathbf{x}} = U_{\mathbf{x},1} U_{\mathbf{x}+\mathbf{e}_1,2} U_{\mathbf{x}+\mathbf{e}_2,1}^\dagger U_{\mathbf{x},2}^\dagger$ is applied to $|\mathbf{s}_0\rangle$, yielding $|\mathbf{s}_1\rangle = P_{\mathbf{x}}^t |\mathbf{s}_0\rangle$, where t is a random integer in $[1, N-1]$ for \mathbb{Z}_N gauge group. This procedure inherently preserves the gauge constraint, ensuring $|\mathbf{s}_1\rangle$ remains physical. The Metropolis algorithm (as described previously) then determines whether $|\mathbf{s}_1\rangle$ is accepted into the Markov chain. For systems with dynamic matter fields, local updates are additionally performed on both gauge and matter configurations living on links, following $|\mathbf{s}_1\rangle = c_{\mathbf{x}}^\dagger U_{(\mathbf{x},\alpha)} c_{\mathbf{x}+\mathbf{e}_\alpha} |\mathbf{s}_0\rangle$.

To accelerate sampling, all plaquettes and links are updated sequentially rather than randomly. This approach significantly reduces computational costs from $O(N_{\text{site}}^2)$ to $O(N_{\text{site}})$ [43]. In pure gauge systems, updates focus exclusively on plaquettes, only involving gauge configurations. When matter fields are present, horizontal and vertical links are sequentially visited to update matter and gauge configurations, after each plaquette sweep over the lattice. After completing a full lattice sweep for plaquettes and links (termed a Monte Carlo sweep), physical observables are measured using the current configuration [43].

S-3. Calculation of Wilson loop operators

The Wilson loop operator W is evaluated along a closed square path of dimensions $\tilde{L} \times \tilde{L}$. As illustrated in the left panel of Fig. S1 for a 3×3 lattice (red lines), this operator takes the form

$$W = U_1 \otimes \cdots \otimes U_6 \otimes U_7^\dagger \otimes \cdots \otimes U_{12}^\dagger,$$

acting on the gauge field variables along the closed contour. Its expectation value $\langle W \rangle$ can be efficiently computed via Monte Carlo sampling. For an $L \times L$ lattice, we select a series of concentric $\tilde{L} \times \tilde{L}$ closed paths and calculate $\langle W \rangle$ for each path, where S denotes the area enclosed by the loop.

In pure \mathbb{Z}_2 lattice gauge theory, the Wilson loop exhibits distinct scaling behaviors across phases: perimeter-law scaling in the deconfined phase and area-law scaling in the confined phase. This transition can be quantified through

the string tension σ , obtained from the scaling relation $\langle W \rangle \propto e^{-\sigma S}$. We determine σ by performing linear fittings on $\ln \langle W \rangle$ versus S , as shown in the right panel of Fig. S1 based on the 32×32 lattice. The evolution of σ with g/h clearly demonstrates a phase transition between the deconfined regime (small σ) and confined regime (large σ).

In addition, for \mathbb{Z}_2 gauge theory coupled to hard-core bosons, in the main text we employ different bulk region definitions to estimate thermodynamic-limit energies [43]. Specifically, the blue contour in Fig. S1(left) demarcates a central $(L-2) \times (L-2)$ region, while the red contour corresponds to a $(L-4) \times (L-4)$ region. By analyzing these progressively smaller bulk regions across varying lattice sizes $L \times L$, we perform systematic finite-size extrapolations, as shown in the main text.